Preprint Title	An advanced structural characterization of templated meso-macroporous carbon monoliths by small- and wide-angle scattering techniques
Authors	Felix Badaczewski, Marc Loeh, Torben Pfaff, Dirk Wallacher, Daniel Clemens and Bernd Smarsly
Publication Date	01 Okt 2019
Article Type	Full Research Paper
Supporting Information File 1	Supporting Information_BJNANO.docx; 22.4 KB
ORCID® iDs	Felix Badaczewski - https://orcid.org/0000-0002-3648-0275; Bernd Smarsly - https://orcid.org/0000-0001-8452-2663

An advanced structural characterization of templated meso-macroporous carbon monoliths by small- and wide-angle scattering techniques

Felix M. Badaczewski[1], Marc O. Loeh[1,2], Torben Pfaff[1], Dirk Wallacher[3], Daniel Clemens[3] and Bernd M. Smarsly*[1,4]

Address: [1]Institute of Physical Chemistry, Justus Liebig University, Heinrich-Buff-Rung 17, 35492 Giessen, Germany [2]Schunk Carbon Technology GmbH, Rodheimer Straße 59, 35452 Heuchelheim, Germany, [3]Helmholtz-Zentrum Berlin für Materialien und Energie, Hahn-Meitner-Platz 1, 14109 Berlin, Germany and [4]Center for Materials Research (LaMa), Justus-Liebig-University, Heinrich-Buff-Ring 16, 35392 Giessen, Germany

Email: Bernd M. Smarsly– bernd.smarsly@phys.chemie.uni-giessen.de

* Corresponding author

Abstract

This study is dedicated to link the nanoscaled pore space of carbons, prepared by hard-templating of meso-macroporous SiO_2 monoliths, to the corresponding nanoscaled polyaromatic microstructure. Two different carbon precursors were used, which generally exhibit markedly different carbonization properties, i.e. a graphitizable pitch and a non-graphitizable resin. The micro- and mesoporosity of these monolithic carbons was studied by the sorption behaviour of a relatively large organic molecule (para-xylene) in comparison to typical gas adsorbates (Ar). In addition, to obtain a detailed view on the nanopore space small-angle neutron scattering (SANS) combined with in-situ physisorption was applied, using deuterated p-xylene (DPX) as a contrast-matching agent in the neutron scattering process. The impact of the carbon precursor on the structural order on an atomic scale in terms of the size and the disorder of the carbon microstructure, on the nanopore structure and on the template process is analysed by special evaluation approaches for SANS and wide-angle X-ray scattering (WAXS). The WAXS analysis shows that the pitch-based monolithic exhibits a more ordered microstructure consisting of larger graphene stacks and similar graphene layer sizes compared to the monolithic resin. Another major finding is the discrepancy in the accessible micro/mesoporosity between Ar and deuterated p-xylene, which was found for the two different carbon precursors (pitch, resin), which can be regarded as representatives in regard to carbon precursors in general. These differences essentially indicate that physisorption using probe gases such as Ar or N_2 can provide misleading parameters if to be used to appraise the accessibility of the nanoscaled pore space.

Keywords

Small-angle neutron scattering; pore structure; carbon; microstructure; adsorption

Introduction and Motivation

Porous sp^2 carbon materials are frequently used in diverse applications like supercapacitors or batteries for the storage of electric energy, as filters for purification of air or water and in adsorption processes [1-8]. The turbostratic microstructure of these “non-graphitic” carbons combined with variable conductivity and a significant nanoscaled, disordered porosity are typical features of this kind of carbon materials, enabling applications in which these particular properties are beneficial. Templating strategies are meanwhile well established to endow carbon with defined porosity on the nanometer scale, in particular to enhance the surface area and to control the pore size [9-12]. This study is dedicated to a quantitative determination of the porosity, e.g. the pore size, volume and pore shape of carbons prepared by hard-templating of meso-macroporous SiO_2 monoliths, and to linking these parameters to the corresponding nanoscaled polyaromatic microstructure. Usually, temperature treatment at elevated temperatures needs to be applied to carbonize molecular organic substances, but the commonly applied temperatures of ca. 800 - 3000 °C can markedly affect the nanoscaled porosity [13-21]. Hence, a combined in-depth elucidation of meso/microporosity and concomitantly the graphene-based structure upon heat treatment is pursued in this study to obtain a profound understanding on the relationship between the changes in the nanopore space and the building blocks surrounding them.

In essence, the structure of “non-graphitic carbons” consists of hexagonal graphene layers, which are stacked in a parallel way, but do not possess 3D long-range crystallographic order, which is referred to as “turbostratic” arrangement. These graphene stacks represent the basic structural unit (BSU) of non-graphitic carbon

materials and exhibit a low packing density [22-25]. The microporosity (pores < 2 nm) results from the imperfection in the packing of the graphene stacks and should thus be dependent on the degree of disorder in the material, i.e. the more disordered a material is, the higher the micropore volume is expected. As with higher carbonization temperature the graphenes as well as their stacking become more ordered, the meso/microporosity is expected to be dependent on the heat treatment temperature.

The degree of disorder in the graphene stacks can be determined by evaluating wide-angle X-ray (WAXS) and neutron (WANS) scattering data of turbostratic carbons. Several current evaluation methods for WAXS and WANS are based on the fitting of entire WAXS/WANS data sets using suitable theoretical scattering functions under variation of structural parameters [26-30]. Here we apply Ruland's and Smarsly's model allowing for the in-depth evaluation of such scattering data, which describe the carbon microstructure on an Angstrom scale [31-34].

In addition, a dependency of the porosity on the precursor materials is expected as some materials are better graphitizable than others. For instance, resin-based carbons are not graphitizable carbons, while pitch-based carbons develop a comparably high structural order upon heat treatment and can be converted into graphite.

The main approaches to influence the carbon structure are the choice of the carbon precursor and the applied heat treatment temperature for carbonization or graphitization. These two factors have the highest impact on the resulting sp^2 microstructure. Since the porosity mainly consists of microporosity additional approaches are necessary to further introduce mesoporosity or macroporosity and to tune the pore system. Chemical and physical activation, using reactive agents like bases (KOH) or gases (CO_2), are only capable to enhance the microporosity by etching the carbon skeleton [35, 36]. To create meso- or marcopores into the carbon system

templating approaches have become a routine strategy. One prominent attempt is hard templating based on silica monoliths with a bimodal pore size distribution (meso- and macropores) and a hierarchical pore network [37-41]. The SiO_2 solid is impregnated with a liquid or dissolved carbon precursor, and thus the carbonization of the precursors takes place within the pores. Template removal is typically performed with concentrated aqueous solutions of NaOH or HF. The hierarchical pore system and the bimodal distribution of pore sizes provide high surface areas and a high permeability. Due to big macropores the material can achieve high flow rates for separation processes, and the mesopores within the walls of the macropores lead to a high surface area, which is beneficial for adsorption processes [42, 43]. Carbon replicas based on silica monoliths are potential candidates for lithium or lithium-sulfur-battery-systems, in which the carbon acts as a conductive matrix [44-46]. Another important factor for these kinds of applications is the connectivity and the accessibility of the pore network. The connection between large and small pores can lead to unfavourable bottlenecks. These narrow bottlenecks can act as a barrier for larger molecules, which block the pore access and lower the pore connectivity. Therefore, we want to investigate the adsorption behaviour of monolithic carbons for larger molecules in comparison to typical gas adsorbates like nitrogen, argon, krypton or carbon monoxide. We chose para-xylene as an adsorbate for vapor sorption to address the sorption at room temperature.

To obtain a detailed view on the nanopore space small-angle neutron scattering (SANS) combined with in-situ physisorption were the methods of choice. Deuterated p-xylene (DPX) acts as a contrast-matching agent in the neutron scattering process. In a perfect case, that is if DPX is capable to fill all pores, the scattering contrast would be zero and the SANS intensity would vanish. Hence, performing SANS coupled with an in-situ physisorption experiment allows for investigating the pore-filing process. In

this study we compare the pore network of different carbon monoliths in an empty state and a filled state. The SANS data were analysed quantitatively in terms of pore size, porosity, wall thickness and angularity of the pores. In addition, the approach of the chord-length distribution (CLD) is used [47-51].

Another question we want to address is the impact of the carbon precursor on the structural order on an atomic scale in terms of the size and the disorder of the carbon microstructure, on the nanopore structure and on the template process. A graphitizable pitch and a non-graphitizable resin, also called glassy carbon is used for comparison. Glassy carbons are derived from thermally processed phenolic formaldehyde resins, which often exhibit a closed porosity (voids). Resins are important compounds in the production of many carbon materials, e.g. as binder matrix for carbon fiber reinforced carbons (CFRC), a light-weight material with excellent mechanical properties even at high temperatures. Upon heat treatment, the PF resin is thereby gradually transformed into a non-graphitizing glassy carbon, consisting of highly crosslinked graphene stacks, which form highly porous ribbon like structures [52-55]. Key properties of glassy carbons, such as thermal conductivity, the chemical resistance, the hardness, the density and the coefficient of thermal expansion are closely related to the carbon microstructure and the porosity. Resin-based carbons are known to possess a substantial content of inaccessible voids on the nanometer scale, in addition to accessible pores [56-58]. Thus, in-situ SANS experiments can help to differentiate between the inaccessible and accessible voids in such template carbons. Here, we compare templated carbons treated at 800 °C and 3000 °C, for which in-situ SANS experiments were performed comparing the evacuated samples with the filled state. A temperature of 3000 °C was chosen, as at such treatment temperature graphitized carbon forms, which possesses advantageous properties such as high electronic

conductivity. The porosity of such materials having undergone a treatment at lower temperatures was also addressed by us in a recent study [59].

The microstructure of both carbons is investigated by an advanced wide-angle X-ray scattering approach. Since standard scattering evaluation methods like single-peak analysis or Rietveld refinement suffer from the turbostratic arrangement of the carbon stacks and do not achieve meaningful results, a novel approach similar to Rietveld refinement is used [33]. The algorithm of the approach is capable to fit the entire wide-angle scattering curve of turbostratic carbons. Physically meaningful parameter like the graphene layer size L_a, the stack size L_c, the carbon bond length l_{cc}, the layer distance a_3 and disorder parameter describing the disorder within the layers (σ_1) and between the layers (σ_3) are directly quantified and can be compared to each other.

All in all, in this study advanced structural characterization methods are used to quantify the microstructure and pore structure of carbon monoliths based on different kinds of carbon precursors, namely a graphitizable pitch and a non-graphitizable resin. This coherent analysis helps to understand the impact of the precursor on the templating process and the final porosity, in relation to the sp^2 microstructure formation.

Results and Discussion

Characterization of the pore system

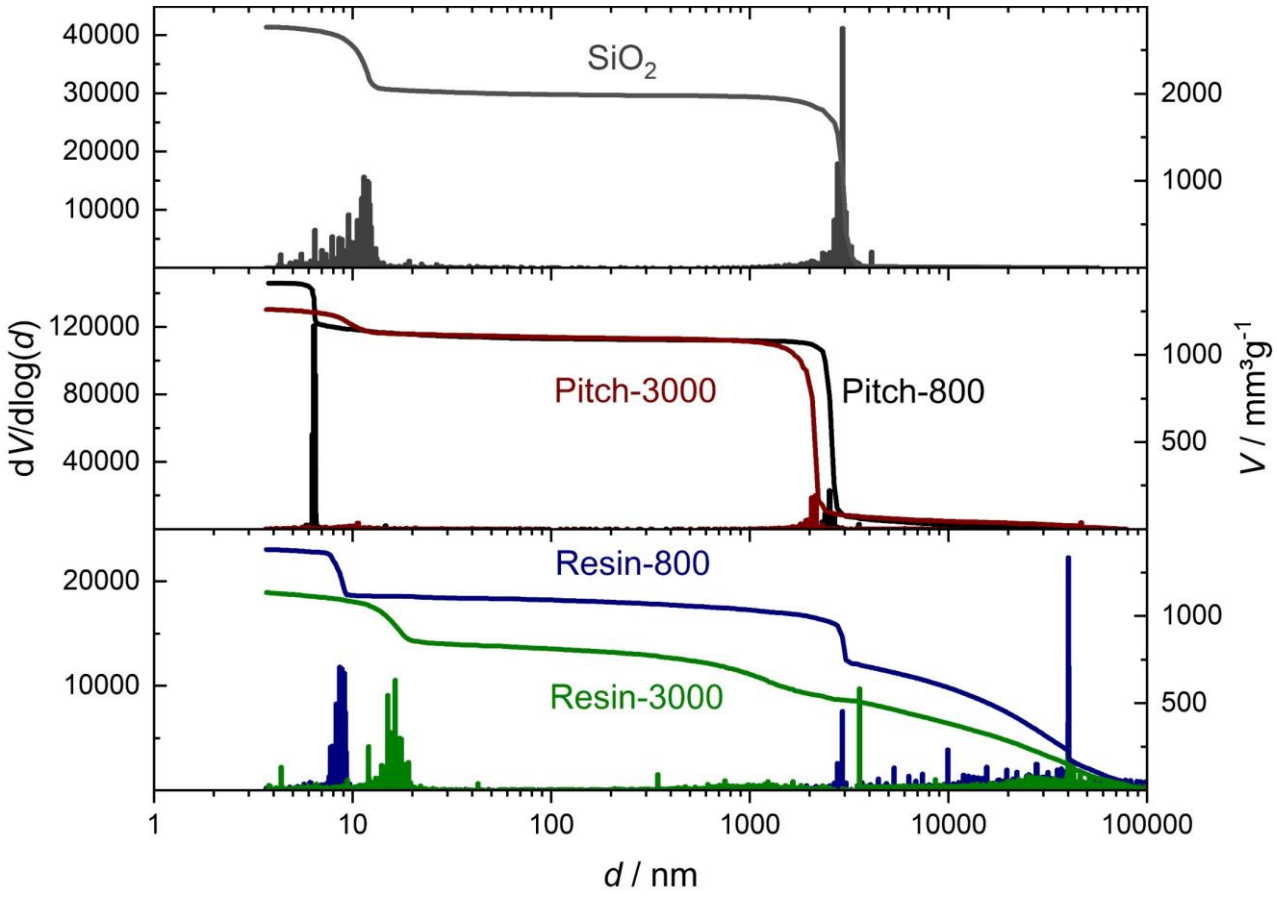

Figure 1: Mercury intrusion porosimetry (MIP) data of the pristine meso-macroporous SiO_2 monolith (top) and the templated carbons, treated at 800 °C and 3000 °C.

This study is focused on four different hard-templated carbon monoliths based on pitch and resin as carbon precursor. In both cases, the hard-templated carbon was exposed to two substantially different temperatures, namely 800 °C and 3000 °C. This means that two porous carbons were treated at 800 °C and two at 3000 °C. In short, in the hard-templating process the pristine silica monoliths were infiltrated by a liquid coal-tar pitch (“Pitch”) or a liquid resole (“Resin”). The carbonization was conducted under nitrogen atmosphere and at a maximum heat treatment temperature of 800 °C. The SiO_2 template was etched by exposure to hydrofluoric acid, and the graphitization took

place in an Acheson furnace at 3000 °C. The bimodal meso-macropore structure of these four carbon materials as well as the meso-macroporous SiO_2 monolith template was investigated by mercury intrusion porosimetry (MIP, Figure 1), scanning electron microscopy (SEM, Figure 2) and physisorption (Figure 3). The initial bimodal pore size distribution of the SiO_2 features mesopores of 13 nm and macropores of 2 µm in diameter (Figure 1). In the case of the pitch-based sample, carbonized at 800 °C (black), the mesopore size of 7 nm is smaller comparted to the initial template, corresponding to the average thickness of the walls separating the mesopores in the original SiO_2 monolith. A slight shrinkage in macropore size from 3 µm to 2 µm is observable for the graphitized pitch sample (Figure 1, Pitch-3000), and a decrease in mesoporosity is observed. Since the macropore dimensions are almost identical in the SiO_2 template and the resulting carbon, the templating process is mainly dominated by a covering of the macropore walls by pitch molecules rather than a complete filling of the macropore space. In case of the mesopores the filling is based on a substantial capillary pressure, thereby capturing the nonpolar liquid precursor within the mesopores.

The macropore size distributions of the monolithic resins are very broad compared to the pitch-based carbons, probably due to experimental issues: The very rigid and stiff resin-based monoliths were crushed by a ball mill in order to fit into the sample holder for MIP measurements. Consequently, interparticular voids appear in the MIP analysis, in addition to the template macroporosity. Nevertheless, the step in the cumulative pore volume at 2 µm is attributable to the dominating macropore size, which corresponds to the dimension expected for the templating of macroporosity. Mesopores of 9 nm in diameter are observed in the resin-based carbon treated at 800 °C, shifting to higher values during heat treatment, contrary to the pitch-based carbon. This increase in the mesopore diameter observed at 3000 °C (Resin-3000) is attributable to the merging

and growth of graphene stacks, which sinter together, thus removing smaller mesopores and leaving behind larger mesopores. Also, the mesopore size distributions of the carbon monoliths at 800 °C are very narrow, which indicates that the SiO_2 walls separating the mesopores exhibit a quite uniform thickness.

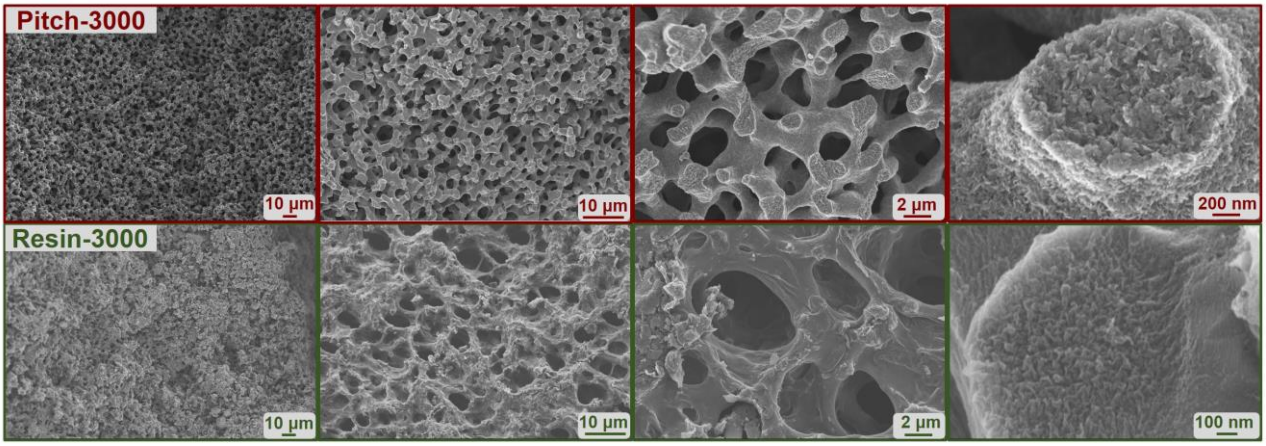

Figure 2: SEM pictures of the pitch-based (top) and resin-based (bottom) monoliths carbonized at 3000 °C.

Figure 2 shows SEM images of the monolithic pitch (red) and resin (green) graphitized at 3000 °C. The sponge-like monolithic structure is remained even at high temperature. The resin-derived carbon monolith displays thicker macropore walls and a less homogenous macropore space, while the macroporosity of the pitch-based carbon monolith looks almost identical to that of the original SiO_2 monolith.

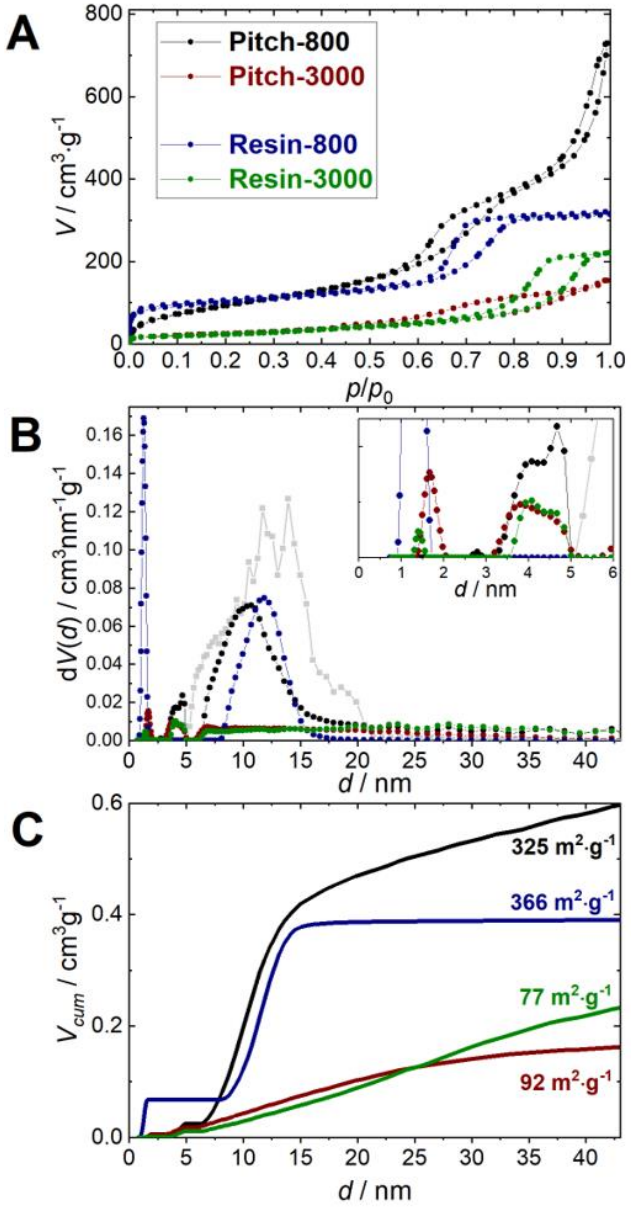

Figure 3: Argon isotherms at 87 K (A), pore-size distributions of the templated carbons and the silica template (B) and cumulative pore volumes (C).

Figure 3 displays Ar isotherms (87 K) and resulting pore size distributions and cumulative pore volumes. All samples show type IVa-isotherms indicating a defined mesopore space [60]. The two replicas carbonized at 800 °C show a narrow mesopore size distribution at around 13 nm (Pitch-800) and 9 nm (Resin-800), and BET surface areas larger than 300 m^2 g^{-1} in both cases. Also, small mesopores (4 nm) and also

micropores are detectable for all samples, while Resin-800 shows pronounced microporosity, which is typical of resin-derived carbons. The heat-treatment at 3000 °C decreases the mesopore volume and surface area significantly for both precursors and the mesopore size distribution broadens substantially. The BET surface area values drop to about 90 $m^2 g^{-1}$ for both carbon precursors at 3000 °C. The micropore volume is slightly larger for Pitch-3000 compared to Resin-3000. One reason for the difference can be closed void in the resin structure, which is inaccessible for Ar atoms.

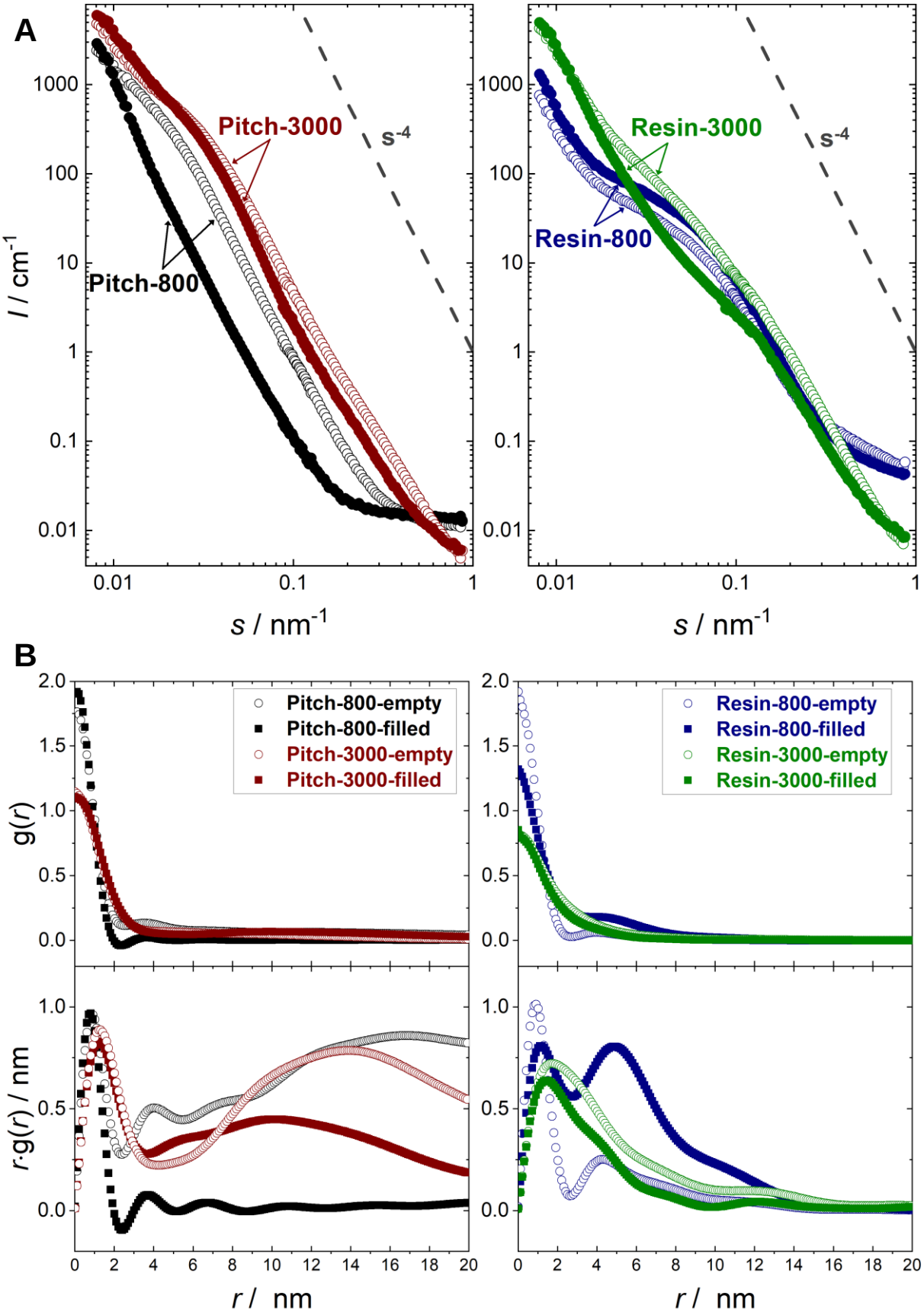

Figure 4: SANS raw data (A) and CLD analysis (B) for the four resin- and pitch-based carbons, treated at 800 °C and 3000 °C. For all samples, SANS analysis was

performed on evacuated samples (hollow symbols), as well as under a maximum load of deuterated p-xylene (filled symbols). All samples exhibit a Porod-asymptote (s^{-4}) at large *s* (modulus of the scattering vector), proving an almost ideal two-phase system (pore – carbon) with sharp interfacial boundaries on the nanometer scale.

Since carbon materials can possess a significant degree of inaccessible voids on the nanoscale, small-angle scattering is a suitable method to determine the overall nanoscaled porosity and hence to determine the fraction of inaccessible voids. Figure 4 displays the acquired SANS data of the monolithic carbons in an empty state and filled with a maximum load of deuterated p-xylene (DPX). The SANS intensity arises due to the contrast of the neutron scattering length density between the carbon matter and the pores and/or voids. Deuterated p-xylene and carbon possess almost identical scattering length densities with respect to neutrons, thereby enabling the principle of “contrast matching”, i.e. micro- and mesopores filled by p-xylene no longer contribute to the SANS pattern, and the filling process can thereby be studied by comparing the filled material with the SANS pattern of the original empty sample. The impact of the graphitization process on the pore sizes is directly observable by comparing the SANS curves in a qualitatively manner. The pitch-based monolith carbonized at 800 °C shows higher SANS intensities in the *s*-range corresponding to microporosity (ca. 0.7 nm^{-1} to 0.9 nm^{1}) compared to the 3000 °C pitch sample. The same trend is observable for the monolithic resins. The resin carbonized at 800 °C shows overall the highest SANS intensity originating from micropores (at large *s* values), which is in good agreement with the physisorption analysis. For the mesoporosity the opposite trend is noticeable, the absolute intensity in the corresponding SANS range increases with heat-treatment temperature, which also meets the physisorption analysis.

Interestingly, the SANS curves of the filled samples do not differ significantly from the curves of the empty samples. The absolute SANS intensity decreases due to the contrast matching adsorbed DPX and the carbon skeleton, but does not vanish as would be expected for a complete filling of the pores. The SANS intensity at very low (ca. 0.008 nm^{-1}) and very high (ca. 0.1 nm^{-1}) *s* values does not change upon exposure to deuterated *p*-xylene, which means small micropores and larger mesopores and macropores are not filled. In contrast, a certain fraction of mesopores between ca. 5 nm and ca. 50 nm is occupied by DPX. These observations are different for the Resin-800 sample. Here, the SANS intensity increases markedly during vapor sorption. A high number of inaccessible voids and sealed porosity hinders the penetration of the pore network, and the adsorption of deuterated *p*-xylene on the external surface leads to a larger scattering contrast, which in turn increases the overall intensity.

The chord-length distributions *g*(*r*) (Figure 4 B) were obtained by fitting the SANS data with a recently introduced parametrisation approach [51]. The CLD evaluation allows the characterization of disordered pore systems and is suitable for two-phase systems, i.e. carbon matter and pores in this case. It provides a distance distribution of two connected phase boundaries. *g*(*r*) consist of contributions of pores and matter and can therefore generally not be directly related to the pore space. The contributions of the matter phase dominate *g*(*r*) for highly porous materials, while *g*(*r*) correlates to the pore space in case of low-porosity materials. In the latter case *g*(*r*) corresponds to a pore size contribution.

The representation *r*·*g*(*r*) is more appropriate to illustrate the dominating length scales, as the first moment of *g*(*r*) (Porod length, *l*p) is defined as $l_p = \int_0^\infty \mathrm{r\,g}(r)\,\mathrm{d}r$. The *r*·*g*(*r*) curves of the pitch-based sample display the filling of mesopores of diameters above ca. 8 nm, i.e. the corresponding contribution decreases from the empty to the filled

state. In the region r < 2 nm no significant decrease is observable, hence no corresponding pores are filled. For the sample Resin-800 the trend is different. Micropores and small mesopores are filled, but the SANS data themselves indicate that only a small fraction of the pores is accessible to DPX. One possible reason is a significant portion of isolated voids, not being accessible for DPX, which is well known for resin-based carbon. Since micropores are filled and mesopores are not, the relative contribution of mesopores to *g(r)* increases.

Table 1 shows parameter directly derived from the SANS data measured in absolute scattering intensities. The parameters are defined in the ESI file (eq. (1) – (10)).

Table 1: Summary of SANS analysis and SANS-derived porosity parameters for the different samples under study.

	Pitch-800-Empty	**Pitch-800-Filled**	**Pitch-3000-Empty**	**Pitch-3000-Filled**	**Resin-800-Empty**	**Resin-800-Filled**	**Resin-3000-Empty**	**Resin-3000-Filled**
Porosity *P*	0.34	0.05	0.11	0.07	0.14	0.14	0.11	0.05
Porod length l_p / nm Eq. (6) (ESI)	4	2	3	5	1	3	2	2
$l_{p,g(r)}$ / nm Eq. (5) (ESI)	4	1	3	4	1	2	2	2
***Angularity g*(0)**	1.8	1.9	1.1	1.1	1.9	1.3	0.8	0.9
Average pore size l_{pores} / nm	7	2	4	6	1	3	2	2

Average wall dimension l_{matter} / nm	1.3	4.2	4.4	12	0.6	1.7	4.7	9.3
Average stack height $L_{c,WAXS}$ / nm	1.2		n.a.		0.9		n.a.	
***Surface S/V* / $m^2 \cdot cm^{-3}$**	305	92	85	29	649	228	81	42
Polydispersity in the pore shape k_l	2	4	2	4	4	1	2	3

The porosity *P* decreases due to the DPX adsorption except for Resin-800, where closed porosity, inaccessible voids and small micropores hinder the penetration of the pore network by DPX. The porosity of the sample Pitch-800 is higher compared to the other samples, which is in good agreement with the physisorption results. The pore size distribution determined by physisorption shows the existence of larger mesopores contributing to the porosity. The average chord length l_p (Porod length) was calculated by two approaches, namely from $g(r)$ using the approach eq. (5) (ESI) and from the SANS data themselves suing eq. (6) (ESI) [51, 59]. The two values are in good agreement for all samples, which shows the validity of the two approaches for the elucidation of SANS data. The $g(0)$ value is an indicator for the angularity of pores, where high $g(0)$ values indicate sharp edges. During the heat-treatment from 800 °C to 3000 °C the pore shape gets smoother, since the $g(0)$ values decrease.

The SANS-derived pore sizes l_{pores} of all samples are below 10 nm and do not change significantly during the DPX vapor adsorption, because apparently a large fraction of the voids is inaccessible porosity. The overall average wall dimension l_{matter} increases

due to the adsorption of DPX, proving that adsorption takes place. Interestingly, l_{matter} lies in the range of the graphene stack heights L_c analysed by Wide-Angle X-ray Scattering, WAXS (see next section), meaning the pores are separated only by 1 - 2 graphene stacks and the graphene layers face to the pores. The surface area *S*/*V* decreases during vapor sorption for all samples. Resin-800-empty shows the highest *S*/*V* values due to a high number of voids and micropores. This value is quite high in the filled state, because of inaccessible micro- and mesopores.

An increase in the polydispersity of the pore shape k_l upon DPX sorption, as seen for Pitch-800, indicates that the shape of the pores gets more inhomogeneous due to a not fully homogenous covered adsorption. This surprising finding is attributed to an inhomogeneous distribution of accessible and inaccessible voids. For Resin-800 the parameter k_l decreases, which indicates that the inaccessible pores or closed voids are quite homogenous in their shape.

To further investigate the surface area in terms of accessibility the results from the SANS and physisorption analysis are compared in a semi-quantitatively way. The obtained values of the Argon BET surface (Figure 3 C) and the overall SANS *S/V* surface (Table 1) give insights into the accessibility of the pore network upon adsorption. Figure 5 A shows the proportion of the surface obtained by Argon physisorption in comparison to the overall surface obtained by SANS of the empty samples. This comparison shows that for the Resin 800 sample the SANS derived surface is much higher in contrast to the Ar physisorption. For this sample more than 40 % of the overall surface area is not accessible to an Ar atom.

Figure 5 B shows the surfaces only obtained by SANS analysis in terms of the empty and DPX filled carbon samples. Here the non-accessibility (black) is much more pronounced: the available surface area for DPX adsorption is less than 50 % for all carbon samples.

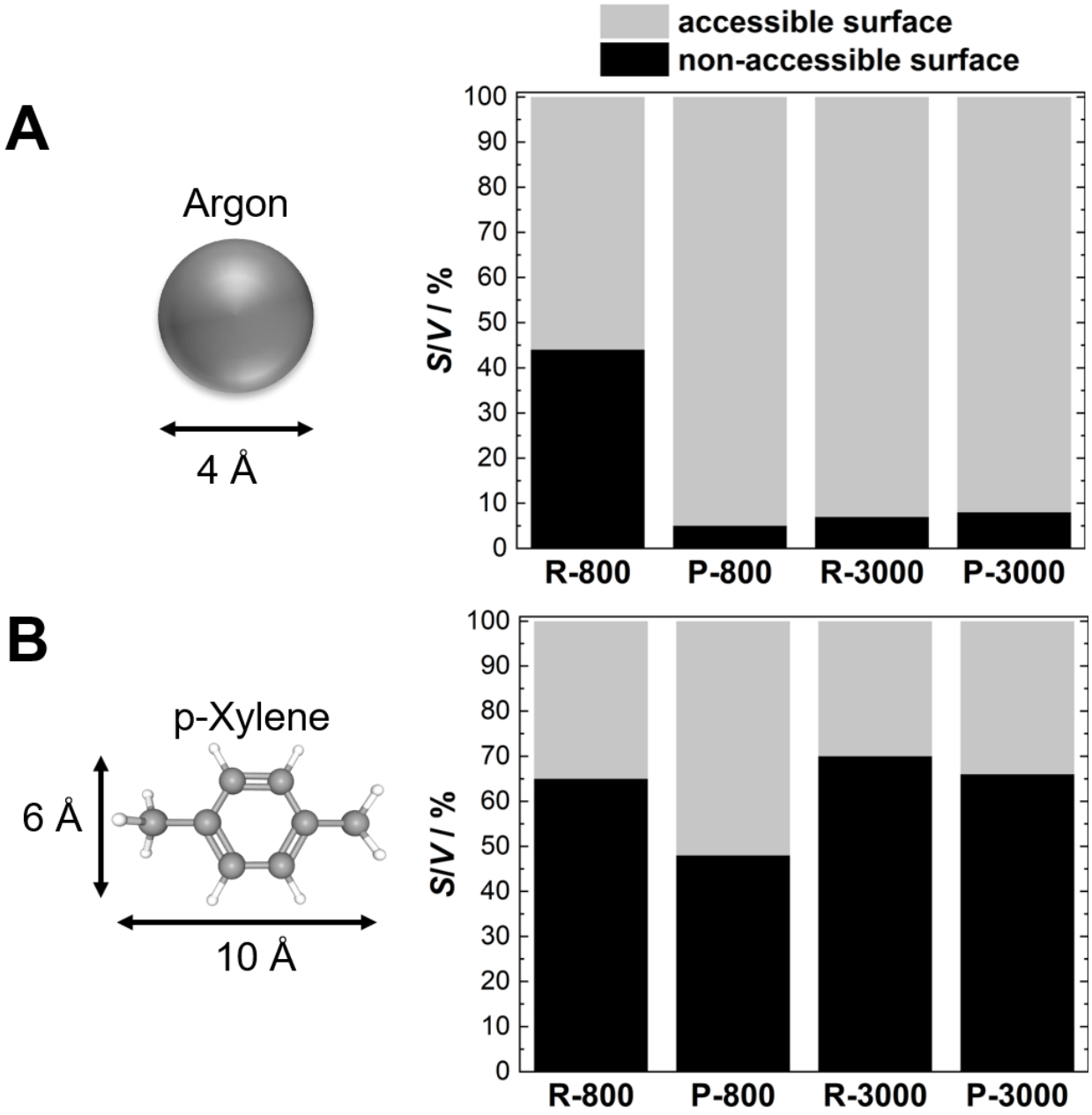

Figure 4: In A the ratios of the surface areas are based on Ar physisorption and SANS analysis (empty samples) ($S_{Phys.,Ar}/S_{SANS,empty}$). In B the ratios are based only on the SANS analysis in terms of the empty and DPX-filled carbon samples ($S_{SANS,filled}/S_{SANS,empty}$).

Microstructural characterization

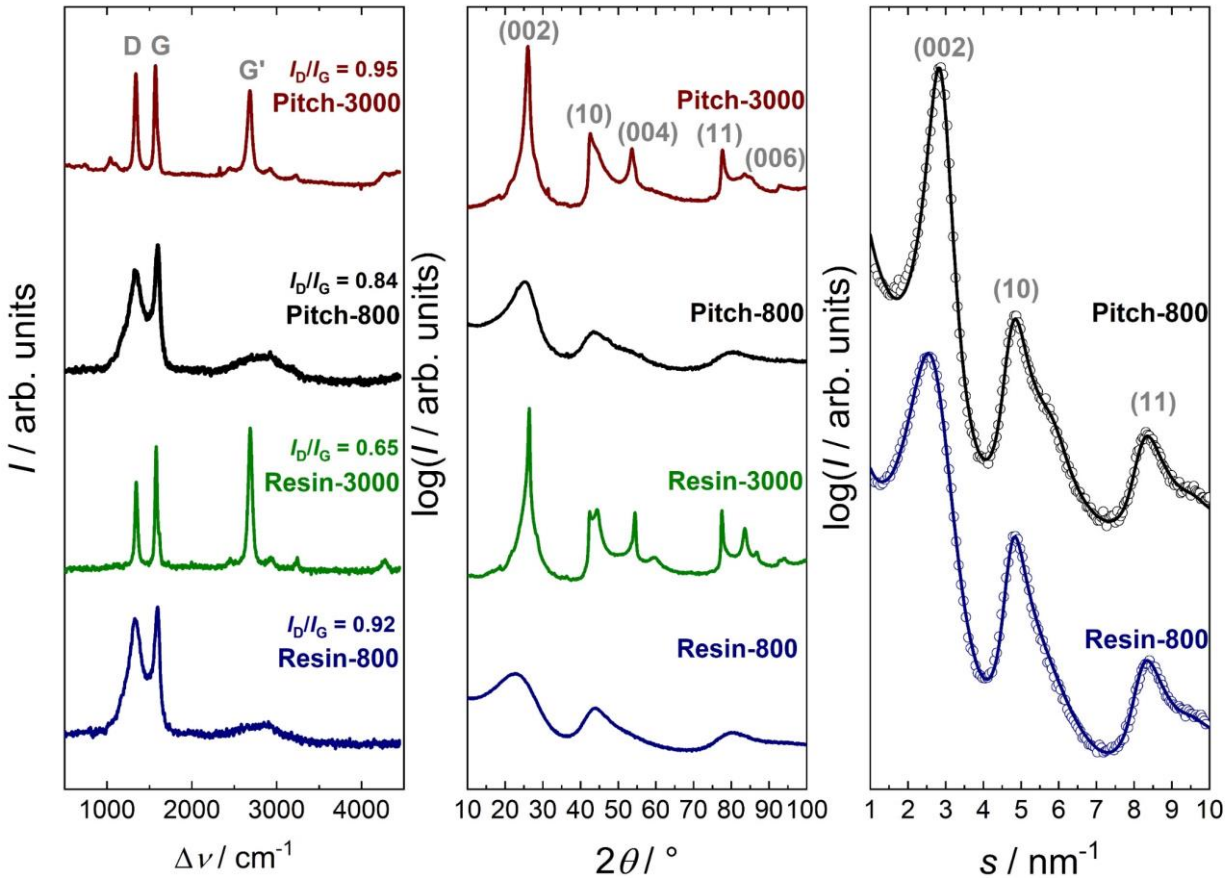

Figure 5: Raman data, WAXS data and fits (lines) of the WAXS data (open circles).

Figure 5 depicts the Raman raw data of the monolithic carbons. The disorder-induced D band arises from breathing vibration of carbon rings and the G band resulted from carbon chains vibrations proof the sp^2 turbostratic microstructure. The G' band is an overtone, where two phonons are involved. It scales with the numbers of layer in a graphene stack. The higher intensity indicates a growth of the stacks. The overlap of the D and G band vanishes at 3000 °C, which is a result of a higher structural order within the graphene layers.

The WAXS data (Figure 5) show the typical scattering maxima of turbostratic carbons. At 800 °C there are only three very broad reflections in the whole 2θ range from 10° to 100° detectable. The (002) reflections arises due to the interlayer scattering between

parallel stacked carbon layers. The (10) and (11) signals arise from the intralayer scattering within the graphene layers. Interestingly, the template resin- and pitch-based samples treated at 3000 °C show no general (*hkl*) reflections as expected for graphite, while the non-templated precursors are converted to graphite at this temperature. This absence of 3D order can be interpreted as attributed to the confinement and nanostructure which hinder the rearrangement and growth of the stacks. We applied the algorithm by Ruland & Smarsly to fit the WAXS data in the whole scattering range and to obtain relevant microstructural parameters. However, the WAXS data of the 3000 °C samples cannot be analysed by such approaches, because the carbon is "graphitic", i.e. the structure is in between a turbostratic carbon and graphite. Additional reflexes in the reflexes in the range of the (10) maxima shine through, which are due to impurities, but are negligible in the analysis. Since the applied model is only applicable for turbostratic carbons, only the 800 °C samples were fitted. The fit of the two scattering curves is in very good agreement with the experimental data, providing reasonable values for different structural parameters (Figure 5). The obtained parameters thus allow a comparison of the two carbon precursors with respect to the graphene stacks (Table 2).

Table 2: WAXS parameter for the pitch- and resin-based carbons. The parameter based on the corresponding non-templated bulk materials are shown in brackets.

	Resin-800	**Pitch-800**	**Resin-3000**	**Pitch-3000**
L_a **/ nm**	1.9 (1.9)	1.6 (1.9)	19 (12)	10 (38)
σ_1	0.14 (0.14)	0.12 (0.14)	-	-
l_{cc} **/ nm**	0.141 (0.141)	0.142 (0.141)	-	-
L_c **/ nm**	0.9 (0.7)	1.2 (1.2)	14 (2.3)	8 (30)
σ_3 **/ nm**	0.071 (0.047)	0.038 (0.027)	-	-
a_3 **/ nm**	0.379 (0.359)	0.350 (0.344)	0.338 (0.340)	0.342 (0.336)
N	2 (2)	4 (4)	41 (7)	29 (89)

Table 2 and Figure 6 show that the graphene layers of the resin (L_a = 1.9 nm) microstructure are slightly larger compared to the pitch (L_a = 1.6 nm). Larger differences occur in the formation of the graphene stacks. By contrast, the stack height L_c is larger (1.2 nm) for the pitch samples compared to the resin samples (0.9 nm). The monolithic resin exhibits only 2 layers per stack on average, which are separated in a rather large distance of 0.379 nm. For the pitch-based monolith, the numbers of layers per stack of the pitch is double as high and the layers in the stacks are packed denser (a_3 = 0.350 nm). Figure 6 shows that the disorder within the graphene sheets (σ_1) and within the stacks (σ_3) of the resin monolith (σ_1 = 0.14, σ_3 = 0.071 nm) is significantly higher compared to the pitch monolith (σ_1 = 0.12, σ_3 = 0.038 nm). A reason for the higher microstructural disorder is the higher content of non-carbon atoms in the resin structure, which hinders the carbonization process and the growth of stacks. Since the resole type of carbon is based on formaldehyde and phenol, a higher oxygen content as well as a higher amount of sp^3-bonded carbon, which connects phenolic groups, is expected. The results show that the pitch-based monolithic exhibits a more ordered

microstructure consisting of larger graphene stacks and similar layer sizes compared to the monolithic resin.

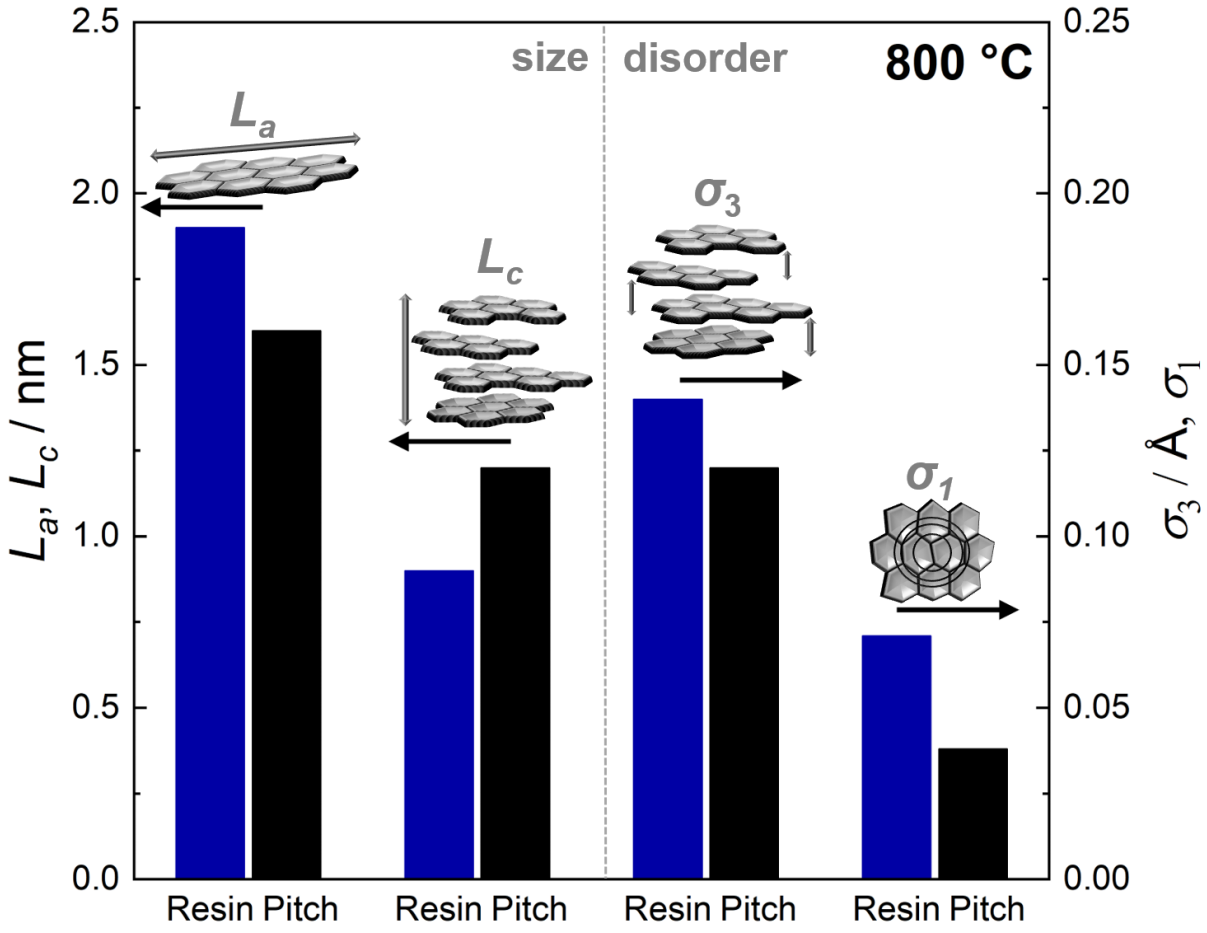

Figure 6: Microstructural parameters describing the size and disorder of the graphene-like structure. The values are based on the templated resin (blue) and pitch (black) carbonized at 800°C.

Conclusion

In this study the hard-templating of carbons using a meso-macroporous SiO_2 scaffold is investigated with respect to the impact of two different, commonly used carbon precursors, namely pitch and resin. In both cases, 800 °C and 3000 °C were applied as heat-treatment temperature, which correspond to the extreme cases of a typical carbonization temperature (800 °C) and a temperature (3000 °C) which usually leads to graphitization. Thus, the investigation of these four carbons allowed for elucidating the impact of temperature-induced carbonization and graphitization on two structural features, namely the porosity and the concomitant evolution of the graphene stacks. The final carbon monoliths were analysed in regard to the relationship between meso- and macroporosity and the sp^2 atomic structure, the latter being determined by the carbon source. Based on porosity analysis (Hg porosimetry and physisorption), small-angle neutron scattering, wide-angle x-ray scattering and Raman spectroscopy we find substantial differences in the porosity between the two types of carbons on all three levels of porosity, i.e. micro-, meso- and macroporosity. While the average macropore sizes are similar, owing to the identical SiO_2 scaffold used, the homogeneity of the macropore space of the resin-derived carbon is lower, probably being a consequence of the polycondensation reaction rupturing the carbonaceous network.

The more interesting disparity pertains to the voids on the nanometer range. For both types of carbons, physisorption analysis reveals mesopores in the range of ca. 7 – 12 nm, which corresponds well to the mesopore space of the SiO_2 hard template. The mesopore size distribution is more defined for the resin-based sample, resembling the one of the SiO_2 monolith, indicating a more precise replication than for the pitch precursor. This finding is plausible, as the resin precursor is smaller than the graphene stacks in pitches. In addition, both carbons contain a certain accessible micropore

volume, which however is considerably smaller than the physisorption-based mesopore volume.

The in-situ SANS experiments using deuterated p-xylene as contrast matching fluid allowed for the quantification of the volume of accessible and inaccessible micro- and mesopores, in relation to the carbon precursor and the heat treatment. Interestingly, a thorough analysis of the SANS data using the chord-length distribution (CLD) concept reveals a subtle picture of these nanometer-sized voids. For the pitch-based porous carbon the average pore size is ca. 7 nm, corresponding well to Ar physisorption analysis. Since SANS probes accessible and inaccessible voids, all mesopores are thus accessible. The pitch precursor exhibits a phase transformation during carbonization at temperatures between 350 °C and 500 °C and forms a liquid-crystal-like state, the lower viscosity of which prevents the formation of closed voids [15]. By contrast, SANS analysis of the empty resin probe (800 °C) provides an average pore size of ca. 1 nm, which is substantially smaller than the average pore size obtained from Ar physisorption. Hence, this the templated resin-based carbon contains a significant concentration of inaccessible voids on the nanometer scale. At 3000 °C the resin-based carbon still contains a considerable content of meso- and micropores, amounting to an accessible micro-mesopore volume of 0.2 mL/g. This quite high porosity is probably due to the fact that resin produces non-graphitizable carbon, i.e. cannot be converted into graphite, even at high temperature. The pores are formed due to the rigid network-like connection of the aromatic groups and the more isotropic arrangement of the resin stacks compared to the anisotropic arrangement of the pitch stacks. Furthermore, the condensation of the resin precursor molecules generates water, which might contribute to the formation of closed voids.

However, surprisingly even the pitch-based carbon does not form graphite, which is counterintuitive as pitches belong to the carbons which usually transform readily into graphite. This inhibition of graphite formation is probably due to the confinement effect of the nanostructure imposed by the nanoscaled porosity. The structural alterations on the nanometer scale are depicted in Fig. 7, emphasizing the relationship between the graphene stacks (size) on the one hand and the changes in the micro-/mesopore size and accessibility on the other hand.

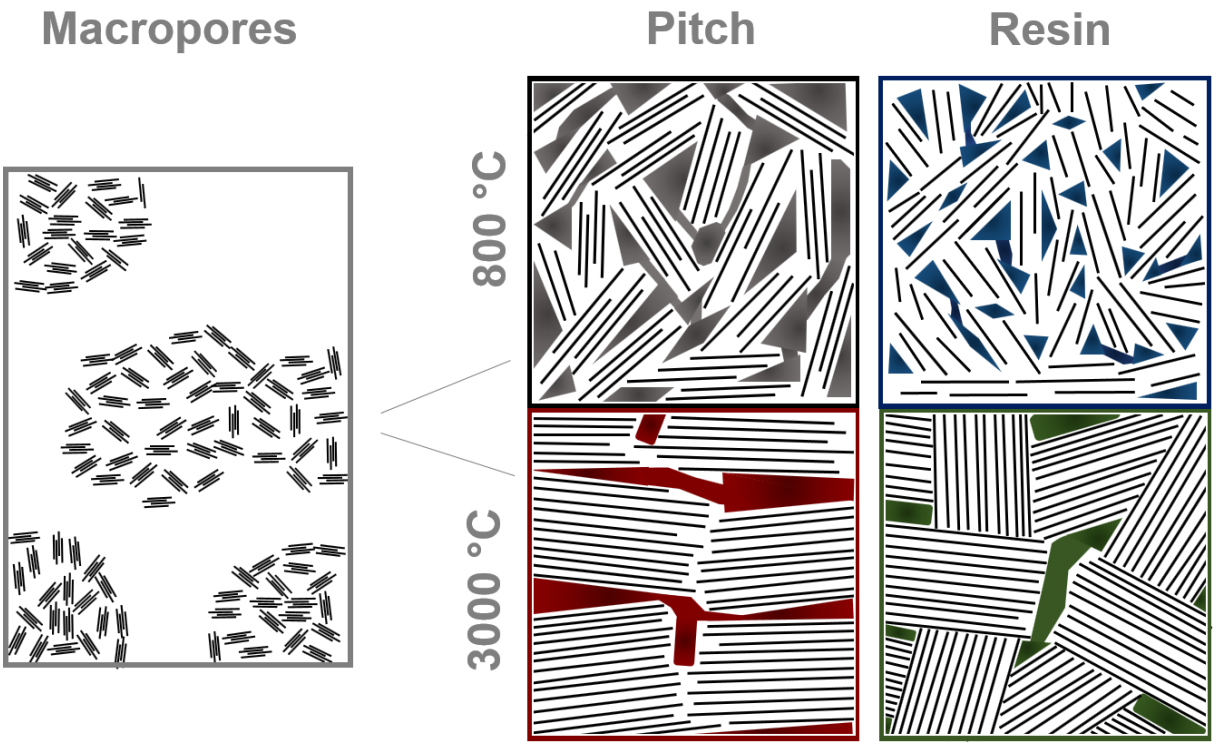

Figure 7: Structural evolution of the different carbons in empty state, in comparison to bulk (i.e. non-templated) resin treated at the same temperatures (800 °C and 3000 °C).

Still, these materials possess a large macropore volume, proving that the templating procedure provides an almost perfect 1:1 copy of the pristine SiO_2 macropore space. Overall, this study provides insight into the evolution of template nanoscaled porosity in carbons in relation to the growth of the graphene stacks and their conversion into graphite. One major finding, which was achieved by the combination of physisorption

and in-situ SANS, from the combination of sorption and SANS is the discrepancy in the accessible micro/mesoporosity between Ar and deuterated p-xylene, the latter serving as representative substance for relevant applications (supercapacitors, filtering). This deviation was found for two different carbon precursors (pitch, resin), which can be regarded as representatives in regard to carbon precursors in general. These differences essentially indicate that physisorption using probe gases such as Ar or N_2 can provide misleading parameters (surface area, volume, pore size) if to be used to appraise the accessibility of the nanoscaled pore space.

Experimental

The synthesis of the silica monolith is based on the Nakanishi process [37,38]. The silica templates were infiltrated by two different carbon precursors, namely a mesophase pitch and a formaldehyde resole. The template removal was done with hydrofluoric acid. Further information can be found in a recent study [41].

SANS data with a very good signal-to-noise-ratio were acquired utilizing the V16 instrument on the cold neutron guide hall of BER-II at the Helmholtz-Zentrum Berlin [61]. Using detector distances of 1.7 m and 11.23 m with the respective chopper and collimator settings resulted in a neutron flux of $2 \cdot 10^6$ $n \cdot cm^{-2} \cdot s^{-1}$. The range of the scattering vector s was from 0.008 nm^{-1} to 0.9 nm^{-1}. Background measurements required for proper data reduction were performed (empty cell, water, Cd-aperture). All samples were measured in DEGAS copper cells, exhibiting a sample volume of 0.2545 cm^3, at 286 K in vacuum (empty) or filled with deuterated para-xylene (DPX, C_8D_{10}) atmosphere (p_0 = 5.7 mbar). The obtained raw data was corrected by subtracting the sample cell backgrounds and reduced by using the software MANTID. An intensity of the scattering data in absolute units of cm^{-1} was achieved.

Ar-physisorption measurements were conducted at 87 K using an AutoSorb iQ instrument coupled with a CryoSync add-on. The samples were outgassed under vacuum at 120 °C for at least 12 hours. The pore-size distributions were calculated by quenched solid-state functional theory (QSDFT) for carbon, using the Quantachrome ASiQwin software and the model “Ar at 87 K on carbons (cylindr./sphere pores QSDFT adsorption branch)”.

Mercury intrusion porosimetry (MIP) measurements were conducted using a Pascal 140/440 from Thermo Scientific.

A scanning electron microscope type Merlin from Zeiss was used to obtain pictures of the monolithic morphologies.

The wide-angle X-ray scattering data were measured with a PANalayitcal X’Pert Pro powder diffractometer. A wavelength λ of 0.15418 nm was used. The 2θ measurement range was from 10° to 100°. A no-background single crystal sample holder made of silicon was used.

Acknowledgements

The authors thank HZB for the allocation of neutron radiation beamtime and thankfully acknowledge the financial support from HZB.

We thank also Dr. Rafael Meinusch and Dr. Martin von der Lehr for mercury intrusion porosity measurements as well as Kevin Turke and Sebastian Werner for performing physisorption measurements.

Financial support is provided by the DFG via the GrK (Research training group) 2204 "Substitute Materials for sustainable Energy Technologies". This project was supported by the Laboratory of Materials Research (LaMa) of JLU.

References

1. Balducci, A.; Dugas, R.; Taberna, P. L.; Simon, P.; Plée, D.; Mastragostinoc, M.; Passerini, S. *J. Pow. So.* **2007**, 165, 922-927.

2. Portet, C.; Taberna, P. L.; Simon, P.; Flahaut, E.; Laberty-Robert, *C. Elect. Acta* **2005**, 50, 4174-4181.

3. Ji, X.; Lee, K. T.; Nazar, L. F. *Nature Materials* **2009**, 8, 500–506.

4. Jayaprakash, N.; Shen, J.; Moganty, S. S.; Corona, A., Archer, L. A. *Angew. Chem. In. Ed.* **2011**, 50, 5904-5908.

5. Radosz, M.; Hu, X.; Krutkramelis, K.; Shen, Y*. Ind. Eng. Chem. Res.* **2008**, 10, 3783-3794.

6. Ao, C. H.; Lee, S. C. *Chem. Engin. Sci.* **2005**, 60, 103 – 109.

7. Reungoat, J.; Escher, B. I.; Macov, M.; Argauda, F. X.; Gernjak, W.; Keller, J. *Water Research* **2012**, 46, 863 – 872.

8. Hameed, B.H.; Din, A. T. M.; Ahmad A. L. *J. Hazard. Mater*. **2007**, 141, 819 – 825.

9. Nishihara, H.; Kyotani, T. *Adv. Mater.* **2012**, 24, 4473–4498.

10. Xia, Y.; Yang, Z.; Mokaya, *R. Nanoscale* **2010**, 2, 639–659.

11. Inagaki, M.; Orikasa, H.; Morishita, T. *RSC Adv.* **2011**, 1, 1620–1640.

12. Inagaki, M., Toyoda, M., Soneda, Y., Tsujimura, S., Morishita, T. *Carbon* **2016**, 107, 448–473.

13. Inagaki, M.; Toyoda, M.; Tsumura, T. *RSC. Adv.* **2014**, 4, 41411–41424.

14. Oberlin, A. *Carbon* **1984**, 22, 521–541.

15. Loeh, M.O.; Badaczewski, F.; Faber, K.; Hintner, S.; Bertino, M. F.; Mueller, P.; Metz, J.; Smarsly, B. M. *Carbon* **2016**, 109, 823–835.

16. Bonnamy, S. *Carbon* **1999**, 37, 1707–1724.

17. Ouzilleau, P.; Gheribi, A. E.; Chartrand, P. *Carbon* **2016**, 109, 896–908.

18. Gadiou, R.; Didion, A.; Saadallah, S.; Couzi, M.; Rouzaud, J. N.; Delhaes, P.; Vix-Guterl, C. *Carbon* **2006**, 44, 3348–3352.

19. Marie, J.; Mering, J. Graphitization of soft carbons. In: Chemistry and Physics of Carbon; Walker Jr., P. L., Ed.; Deker: New York, 1970; Vol. 6, pp 125-189.

20. Auguie, D.; Oberlin, M.; Oberlin, A. *Carbon* **1980**, 18, 337–346.

21 Bonnamy, S. *Carbon* **1999**, 37, 1707–1724.

22. Warren, B. E. *Phys. Rev.* **1941**, 59, 693−698.

23. Fitzer, E.; Kochling, K. H.; Boehm, H. P.; Marsh, H. *Pure Appl. Chem.* **1995**, 67, 473− 506.

24. Franklin, R. E. *Proc. R. Soc. A* **1951**, 209, 196–218.

25. Bourrat, X.; Oberlin, A.; Escalier, J. C. *Fuel* **1986**, 65, 1490–1500.

26. Shi, H.; Reimers, J. N.; Dahn, J. R. J*. Appl. Crystallogr.* **1993**, 26, 827−836.

27. Azuma, H. *J. Appl. Crystallogr.* **1998**, 31, 910−916.

28. Fujimoto, H.; Shiraishi, M. *Carbon* **2001**, 39, 1753−1761.

29. Ruland, W.; Smarsly, B. *J. Appl. Crystallogr.* **2002**, 35, 624−633.

30. Puech, P.; Dabrowska, A.; Ratel-Ramond, N.; Vignoles, G. L.; Monthioux, M. *Carbon* **2019**, 147, 602−611.

31. Faber, K.; Badaczewski, F.; Oschatz, M.; Mondin, G.; Nickel, W.; Kaskel, S.; Smarsly, B. M. *J. Phys. Chem. C* **2014**, 118, 15705−15715.

32. Faber, K.; Badaczewski, F.; Ruland, W.; Smarsly, B. M. *Z. Anorg. Allg. Chem.* **2014**, 640, 3107−3117.

33. Ruland, W.; Smarsly, B. *J. Appl. Crystallogr.* **2002**, 35, 624–633.

34. Pfaff, T.; Badaczewski, F.; Loeh, M. O.; Franz, A.; Hoffmann, J.-U.; Reehuis, M.; Zeier, W. G.; Smarsly, B. M. *J. Phys. Chem. C* **2019**, 123, 20532-20546.

35. Ahmadpour, A.; Do, D. D. *Carbon* **1996**, 34, 471 – 479.

36. Lillo-Ródenas, M. A; Cazorla-Amorós, D.; Linares-Solano, A. *Carbon* **2003**, 41, 267-275.

37. Nakanishi, K., Tanaka, N. *Acc. Chem. Res.* **2007**, 40, 863–873.

38. Nakanishi, K. *J. Porous. Mater.* **1997**, 4, 67–112.

39. Inagaki, M.; Orikasa, H.; Morishita, T. *RSC Advances* **2011**, 1, 1620–1640.

40. Adelhelm, P.; Cabrera, K.; Smarsly, B. M. *Sci. Technol. Adv. Mater.* **2012**, 13, 015010.

41. Loeh, M. O.; Badaczewski, F.; von der Lehr, M.; Ellinghaus, R.; Dobrotka, S.; Metz, J.; Smarsly, B. M. *Carbon* **2018**, 129, 552–563.

42. Doherty, C. M.; Caruso, R. A.; Smarsly, B. M.; Adelhelm, P.; Drummond, C. *J. Chem. Mater.* **2009**, 21, 5300–5306.

43. Kim, Y. S.; Guo, X. F.; Kim, G. *J. Catalysis Today* **2010**, 150, 91–99.

44. Yu, L.; Brun, N.; Sakaushi, K.; Eckert, J.; Titirici, M. M. *Carbon* **2013**, 61, 245-253.

45. Reitz, C.; Breitung, B.; Schneider, A.; Wang, D.; von der Lehr, M.; Leichtweiss, T.; Janek, J.; Hahn, H.; Brezesinski, T. *ACS Appl. Mater. Inter.* **2016**, 816, 10274-10282.

46 Schneider, A.; Weidmann, C.; Suchomski, C.; Sommer, H.; Janek, J.; Brezesinski, T. *Chem. Mater.* **2015**, 275, 1674-1683.

47. Mascotto, S.; Kuzmicz, D.; Wallacher, D.; Siebenbürger, M.; Clemens, D.; Risse, S.; Yuan, J.; Antonietti, M.; Ballauff, M. *Carbon* **2015**, 82, 425–435.

48. Perret, R.; Ruland, W. *J. Appl. Crystallogr.* **1972**, 5, 183–187.

49. Perret, R.; Ruland, W. *J. Appl. Crystallogr.* **1968**, 1, 308–313.

50. Ruland, W. *J. Appl. Crystallogr.* **2010**, 43, 998–1004.

51. Smarsly, B.; Antonietti, M.; Wolff, T. *J. Chem. Phys.* **2002**, 116, 2618-2627.

52. Harris, P. J. F. *Int. Mater. Rev.* **1997**, 42, 206–218.

53. Tzeng, S. S.; Chr, Y. G. *Mater. Chem. Phys.* **2002**, 73, 162–169.

54. Sharma, S.; Shyam Kumar, C. N.; Korvnik, J. G.; Kübel, C. *Sci. Rep.* **2018**, 8, 16282.

55. Jurkiewicz, K.; Pawlyta, M.; Zygadło, D.; Chrobak, D.; Duber, S.; Wrzalik, R.; Ratuszna A.; Burian A. *J. Mater. Sci.* **2018**, 53, 3509–3523.

56. Jenkins, G. M.; Kawamura, K. *Nature* **1971**, 231, 175–176.

57. Jenkins, G. M.; Kawamura, K.; Ban, L. L. *Proc. R. Soc. A.* **1972**, 327, 501–507.

58. Fitzer, E.; Schaefer, W. Carbon 1970, 8, 353–364.

59. Badaczewski, F.; Loeh, M. O.; Pfaff, T.; Dobrotka, S.; Wallacher, D.; Clemens, D; Metz J.; Smarsly, B. M. *Carbon* **2019**, 141, 169-181.

60. Thommes, M.; Kaneko, K.; Neimark, A. V.; Olivier, J. P.; Rodriguez-Reinoso, F.; Rouquerol, J.; Swing, K. S. W. *Pure Appl. Chem.* **2015**, 87, 1051–1069.

61. Vogtt, K.; Siebenbürger, M.; Clemens, D., Rabe, C.; Lindner, P.; Russina, M.; Fromme, M.; Mezei, F.; Ballauff, M. *J. Appl. Cryst.* **2014**, 47, 237-244.